Available online at www.sciencedirect.com
SCIENCE DIRECT®
Journal of Computational Physics 198 (2004) 645–658
JOURNAL OF COMPUTATIONAL PHYSICS
www.elsevier.com/locate/jcp

Fully dispersive nonlinear water wave model in curvilinear coordinates

S. Beji [a,*], K. Nadaoka [b]

[a] Department of Naval Architecture and Ocean Engineering, Istanbul Technical University, Maslak 34469, Istanbul, Turkey
[b] Graduate School of Information Science and Engineering, Tokyo Institute of Technology, 2-12-1 O-okayama, Meguro-ku, Tokyo 152-8552, Japan

Received 10 September 2003; received in revised form 18 December 2003; accepted 19 December 2003
Available online 27 February 2004

Abstract

A vertically integrated fully dispersive nonlinear wave model is expressed in curvilinear coordinates with non-orthogonal grids for the simulation of broad-banded nonlinear random water waves in regions of arbitrary geometry. The transformation is performed for both dependent and independent variables, hence an irregular physical domain is converted into a rectangular computational domain with contravariant velocities. Use of contravariant velocity components as dependent variables ensures easy and accurate satisfaction of the wall condition for lateral enclosures surrounding a physical domain, such as a coastal area, channel, or harbor. The numerical scheme is based on finite-difference approximations with staggered grids which results in implicit formulations for the momentum equations and a semi-explicit formulation for the continuity equation. Linear long wave propagation in a channel of varying cross-section and linear random wave propagation in a circular channel are presented as test cases for comparisons with the corresponding analytical solutions. Cnoidal and Stokes waves in a circular channel are also simulated as examples to nonlinear wave propagation within curved walls.

AMS: 65M06; 76B15

Keywords: Nonlinear random waves; Dispersion; Curvilinear coordinates

1. Introduction

Beginning from the early 1980s use of boundary-fitted coordinates in the numerical solution of physical problems involving arbitrary geometries has become one of the primary numerical approaches. Experience gained within the last two decades has revealed the most suitable techniques for arranging the transformed governing equations and the most appropriate numerical tools for obtaining the reliable results. Today, the

* Corresponding author. Tel.: +(90)-212-285-6442; fax: +(90)-212-285-6454.
E-mail addresses: sbeji@itu.edu.tr (S. Beji), nadaoka@mei.titech.ac.jp (K. Nadaoka).

0021-9991/$ - see front matter © 2004 Elsevier Inc. All rights reserved.
doi:10.1016/j.jcp.2003.12.022

overall approach to numerical solution of a physical problem in boundary-fitted curvilinear coordinates is more or less a well-established procedure [1,2].

Earlier works on circulation or tidal wave models in curvilinear coordinates considered only the geometrical transformation (i.e., the transformation of the independent variables only) and retained the original Cartesian velocities as dependent variables [3–5]. Besides, orthogonal transformations were preferred as they yielded simpler equations when compared with non-orthogonal transformations. Later studies showed that use of the Cartesian velocities introduces definite numerical restrictions and inaccuracies (see Muin and Spaulding [6] for more details), hence formulations in terms of the contravariant velocities with non-orthogonal grids should be preferable for accuracy and versatility. First use of contravariant velocity variables in a curvilinear circulation model is attributed to Sheng [7].

Androsov et al. [8] expressed long wave equations in curvilinear grids with particular attention to the formulation of the open boundary conditions. A storm surge flooding model based on the long wave equations combined with the wet–dry grid method in curvilinear coordinates was given by Shi et al. [9]. Bao et al. [10] presented a three-dimensional tidal wave model in boundary-fitted coordinates with a σ-stretching in the vertical coordinate and used it for a case study of the Bohai Sea. Recent works of Li and Zhan [11] and Shi et al. [12] on improved Boussinesq models in boundary-fitted coordinates are notable exceptions to non-dispersive wave models. Romanenkov et al. [13] investigated the advantages and disadvantages of different velocity variables and grids in viscous shallow-water equations, and, quite recently, Sankaranarayanan and Spaulding [14] studied the effects of grid non-orthogonality on the numerical results obtained from the shallow water equations in boundary-fitted coordinate systems.

The present work contributes to a rather unexploited application area of the curvilinear coordinate transformations and expresses a fully dispersive nonlinear water wave model, valid for broad-banded random waves, in boundary-fitted curvilinear coordinates in terms of the contravariant velocities. Use of a hyperbolic profile for the vertical distribution of the velocity field in the derivation of the present model provides a significant advantage over the Boussinesq-type dispersive models, which are derived based on a parabolic profile assumption and consequently restricted to limited depths. Furthermore, the dispersive characteristics of the present equations are enhanced by taking more component equations instead of increasing the order of derivatives of the dependent variables as in the Boussinesq-type equations.

Transformation of the wave model is accomplished in the simplest manner possible by recognizing a definite expression which is repeated in slightly different forms in the equations. The second-order radiation condition of Engquist and Majda [15] is also expressed in curvilinear coordinates as outgoing boundary condition. The resulting transformed equations are then numerically solved using finite-difference approximations with staggered girds.

Two test cases are considered for checking the reliability of the numerical scheme. First, linear long wave propagation across a channel of gradually varying cross-section is simulated to compare the amplitude variation along the channel against Green's analytical formula. Then, linear random wave simulation in a circular channel is considered for comparing the numerically obtained solution with the exact analytical solution. Results of the test cases show quite satisfactory agreement between the analytical and the numerical solutions.

As examples to nonlinear wave transformations in arbitrary physical domains, the cnoidal waves and the Stokes waves in a circular channel are simulated. Distinct features of the nonlinear simulations as compared with the linear simulations are emphasized. In closing, comments are made on possible practical applications of the equations presented.

2. Transformation of wave equations

The wave equations used in this work are the fully dispersive nonlinear equations developed by Nadaoka et al. [16]. The model equations are capable of simulating broad-banded nonlinear random waves over

arbitrary water depths as well as reproducing the cnoidal waves and the second-order Stokes waves. The continuity equation and the nth components of the x- and y-momentum equations in Cartesian coordinates are given by

$$\frac{\partial\zeta}{\partial t}+\frac{1}{g}\sum_{m=1}^{N}\left\{\frac{\partial}{\partial x}\left[\left(\frac{\omega_m^2}{k_m^2}+g\zeta\right)u_m\right]+\frac{\partial}{\partial y}\left[\left(\frac{\omega_m^2}{k_m^2}+g\zeta\right)v_m\right]\right\}=0, \tag{1}$$

$$\sum_{m=1}^{N}A_{nm}\frac{\partial u_m}{\partial t}+B_n\frac{\partial}{\partial x}\left[g\zeta+\zeta\frac{\partial w_0}{\partial t}+\frac{1}{2}\left(u_0^2+v_0^2+w_0^2\right)\right]$$
$$=\frac{\partial}{\partial t}\sum_{m=1}^{N}\left\{C_{nm}\frac{\partial}{\partial x}\left(\frac{\partial u_m}{\partial x}+\frac{\partial v_m}{\partial y}\right)+D_{nm}^{x}\left(\frac{\partial u_m}{\partial x}+\frac{\partial v_m}{\partial y}\right)\right\}, \tag{2}$$

$$\sum_{m=1}^{N}A_{nm}\frac{\partial v_m}{\partial t}+B_n\frac{\partial}{\partial y}\left[g\zeta+\zeta\frac{\partial w_0}{\partial t}+\frac{1}{2}\left(u_0^2+v_0^2+w_0^2\right)\right]$$
$$=\frac{\partial}{\partial t}\sum_{m=1}^{N}\left\{C_{nm}\frac{\partial}{\partial y}\left(\frac{\partial u_m}{\partial x}+\frac{\partial v_m}{\partial y}\right)+D_{nm}^{y}\left(\frac{\partial u_m}{\partial x}+\frac{\partial v_m}{\partial y}\right)\right\}, \tag{3}$$

with

$$A_{nm}=\frac{\omega_n^2-\omega_m^2}{k_n^2-k_m^2},\quad A_{nn}=\frac{\omega_n^2+h\left(gk_n^2-\omega_n^4/g\right)}{2k_n^2},\quad B_n=\frac{\omega_n^2}{k_n^2},$$
$$C_{nm}=\frac{(B_n-A_{nm})}{k_m^2},\quad (D_{nn}^{x},D_{nn}^{y})=\frac{E_n}{A_{nn}}\left(3\frac{C_{nn}}{h}+\frac{B_n^2}{g}\right)\left(\frac{\partial h}{\partial x},\frac{\partial h}{\partial y}\right),$$
$$(D_{nm}^{x},D_{nm}^{y})=\frac{4h^{-1}E_m}{\left(k_m^2-k_n^2\right)}\left\{\sqrt{\frac{E_n}{E_m}}-\frac{\left[A_{nm}-\left(k_m^2-k_n^2\right)C_{nm}\right]}{A_{mm}}\right\}\left(\frac{\partial h}{\partial x},\frac{\partial h}{\partial y}\right),$$
$$E_n=A_{nn}-B_n/2,\quad u_0=\sum_{m=1}^{N}u_m,\quad v_0=\sum_{m=1}^{N}v_m,$$
$$w_0=-\frac{1}{g}\sum_{m=1}^{N}\left\{\frac{\partial}{\partial x}[B_m(u_m+v_m)]+\frac{\partial}{\partial y}[B_m(u_m+v_m)]\right\},$$

where g is the gravitational acceleration, ζ is the free surface elevation, u_m and v_m are the mth components of the horizontal velocity vector at the still water level $z=0$. ω_n indicates one of the selected circular frequencies $(n=1,\ldots,N)$ of the equations while k_n denotes the corresponding wave number computed according to the dispersion relation $\omega_n^2=gk_n\tanh k_nh$ for a given local depth h.

Eqs. (1)–(3) provide $2N+1$ equations for the solution of the unknowns ζ and u_m, v_m with $m=1,\ldots,N$. For simple periodic or narrow-banded wave fields just a single component $N=1$ is enough while for broad-banded wave fields taking $N=2$ or $N=3$ is quite sufficient as demonstrated in [16].

Coordinate transformations from a two-dimensional Cartesian system (x,y,t) to a two-dimensional curvilinear system (ξ,η,τ) are given by [2]

$$\frac{\partial}{\partial t}=\frac{\partial}{\partial\tau},\quad \frac{\partial}{\partial x}=\xi_x\frac{\partial}{\partial\xi}+\eta_x\frac{\partial}{\partial\eta},\quad \frac{\partial}{\partial y}=\xi_y\frac{\partial}{\partial\xi}+\eta_y\frac{\partial}{\partial\eta}, \tag{4}$$

in which the metrics are defined as

$$\xi_x = Jy_\eta, \quad \xi_y = -Jx_\eta, \quad \eta_x = -Jy_\xi, \quad \eta_y = Jx_\xi, \tag{5}$$

where $J = (x_\xi y_\eta - x_\eta y_\xi)^{-1}$ is the Jacobian of the transformation. A subscript indicates partial differentiation with respect to the denoted variable. A sketch of an arbitrary physical domain and the corresponding physical domain is given in Fig. 1.

A careful examination reveals that the expression

$$F = \frac{\partial}{\partial x}(fu_m) + \frac{\partial}{\partial y}(fv_m), \tag{6}$$

where f is a scalar function, occurs repeatedly in Eqs. (1)–(3). That is, $f = (\omega_m/k_m)^2 + g\zeta$ in Eq. (1) and $f = 1$ in Eqs. (2) and (3). Therefore, expressing F in curvilinear coordinates in terms of the contravariant velocity components is necessarily the first step. Making use of Eqs. (4) and (5), denoting the mth components of the contravariant velocities in the ξ- and η-directions by U_m and V_m while noting that they are defined as

$$U_m = \xi_x u_m + \xi_y v_m \quad \text{and} \quad V_m = \eta_x u_m + \eta_y v_m \tag{7}$$

gives, after some straightforward algebra

$$F = \frac{\partial}{\partial x}(fu_m) + \frac{\partial}{\partial y}(fv_m) = J\left[\frac{\partial}{\partial \xi}\left(fU_m^*\right) + \frac{\partial}{\partial \eta}\left(fV_m^*\right)\right], \tag{8}$$

where U_m^* and V_m^* are defined as $U_m^* = U_m/J$ and $V_m^* = V_m/J$ for notational and numerical convenience.

The continuity equation is now readily transformed by simply setting $f = (\omega_m/k_m)^2 + g\zeta$ in (8) and then using it back in Eq. (1). On the other hand, setting $f = 1$ in (8) gives the terms multiplied by C_{nm} and D_{nm} in the momentum equations. The surface velocities u_0, v_0, and w_0 may be computed directly by solving u_m and v_m in terms of U_m^* and V_m^*

$$u_m = \eta_y U_m^* - \xi_y V_m^* \quad \text{and} \quad v_m = -\eta_x U_m^* + \xi_x V_m^*. \tag{9}$$

The final step is to combine the x- and y-momentum equations in appropriate manner to obtain the corresponding momentum equations in the ξ- and η-directions. To this end, multiplying (2) by ξ_x, (3) by ξ_y, and adding the resulting equations give the ξ-momentum equation. In a similar vein, multiplying (2) by η_x,

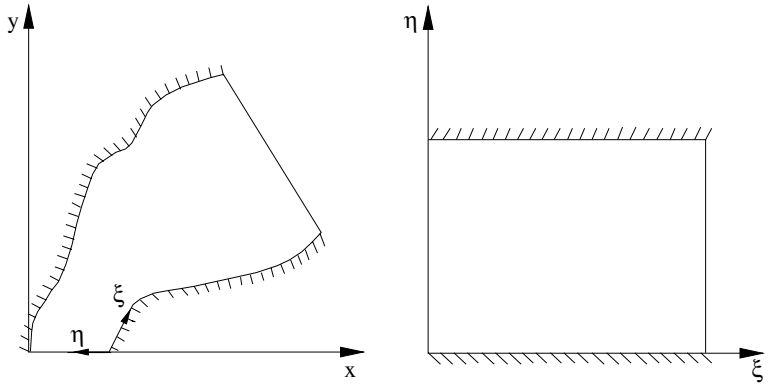

Fig. 1. Definition sketch of an arbitrary physical domain (left) and the corresponding computational domain (right). The hatched lines indicate wall boundaries.

(3) by η_y, and adding give the η-momentum equation. Thus, the wave model in curvilinear coordinates in terms of the contravariant velocity components $U_m^* = U_m/J$ and $V_m^* = V_m/J$ becomes

$$\frac{\partial \zeta}{\partial \tau} + \frac{J}{g}\sum_{m=1}^{N}\left\{\frac{\partial}{\partial \xi}\left[\left(\frac{\omega_m^2}{k_m^2} + g\zeta\right)U_m^*\right] + \frac{\partial}{\partial \eta}\left[\left(\frac{\omega_m^2}{k_m^2} + g\zeta\right)V_m^*\right]\right\} = 0, \tag{10}$$

$$\sum_{m=1}^{N} JA_{nm}\frac{\partial U_m^*}{\partial \tau} + B_n\left[\left(\xi_x^2 + \xi_y^2\right)\frac{\partial Q}{\partial \xi} + \left(\xi_x\eta_x + \xi_y\eta_y\right)\frac{\partial Q}{\partial \eta}\right] = \sum_{m=1}^{N} C_{nm}\left[\left(\xi_x^2 + \xi_y^2\right)\frac{\partial^2 W_m^*}{\partial \xi \partial \tau} + \left(\xi_x\eta_x + \xi_y\eta_y\right)\frac{\partial^2 W_m^*}{\partial \eta \partial \tau}\right] + \sum_{m=1}^{N}\left(\xi_x D_{nm}^x + \xi_y D_{nm}^y\right)\frac{\partial W_m^*}{\partial \tau}, \tag{11}$$

$$\sum_{m=1}^{N} JA_{nm}\frac{\partial V_m^*}{\partial \tau} + B_n\left[\left(\eta_x^2 + \eta_y^2\right)\frac{\partial Q}{\partial \eta} + \left(\xi_x\eta_x + \xi_y\eta_y\right)\frac{\partial Q}{\partial \xi}\right] = \sum_{m=1}^{N} C_{nm}\left[\left(\eta_x^2 + \eta_y^2\right)\frac{\partial^2 W_m^*}{\partial \eta \partial \tau} + \left(\xi_x\eta_x + \xi_y\eta_y\right)\frac{\partial^2 W_m^*}{\partial \xi \partial \tau}\right] + \sum_{m=1}^{N}\left(\eta_x D_{nm}^x + \eta_y D_{nm}^y\right)\frac{\partial W_m^*}{\partial \tau}, \tag{12}$$

in which

$$W_m^* = J\left(\frac{\partial U_m^*}{\partial \xi} + \frac{\partial V_m^*}{\partial \eta}\right), \quad Q = g\zeta + \zeta\frac{\partial w_0}{\partial t} + \frac{1}{2}\left(u_0^2 + v_0^2 + w_0^2\right).$$

The coefficients A_{nm}, B_n, C_{nm} remain as previously defined; only h_x and h_y appearing in D_{nm}^x and D_{nm}^y need to be computed as $\xi_x h_\xi + \eta_x h_\eta$ and $\xi_y h_\xi + \eta_y h_\eta$.

3. Boundary conditions

A typical problem requires basically three different boundary conditions: incoming boundary condition, wall condition, and outgoing boundary condition. While the first two conditions are easily handled, the radiation boundary condition requires the transformation process applied to the wave equations.

At the incoming boundary, which is taken along the η-axis at $\xi = 0$, the free surface displacement ζ is specified by assigning time series of a definite wave form. For unidirectional waves, U_m^* is obtained from the relation $U_m^* = (\xi_x u_m + \xi_y v_m)/J$, using $u_m = C\zeta/(\omega_m^2/gk_m^2 + \zeta)$ and $v_m = 0$, as dictated by the nonlinear continuity equation for unidirectional periodic waves of celerity $C = \omega/k$, which, for nonlinear waves, may be different from ω_m/k_m used in wave equations. Directional waves at the incoming boundary may also be generated by using these specifications, it is only necessary to introduce an appropriate phase angle for each grid point along the η-axis on the boundary.

Since the wave model is formulated in terms of the contravariant velocities, the wall condition even for irregular geometries can be specified in the most straightforward manner by simply requiring the contravariant velocity component normal to the wall boundary vanish.

Implementation of the outgoing boundary condition in the numerical scheme requires the transformation of an appropriate radiation equation to the curvilinear coordinates. Problems associated with the artificial reflection of waves from the outgoing boundaries have resulted in a variety of proposed boundary conditions. For water waves the second-order boundary condition of Engquist and Majda [15] proves particularly good for the absorption of directional waves and contains Sommerfeld's classical radiation

condition as special case. For waves moving primarily in the x- and y-directions, respectively, their second-order condition gives

$$\frac{\partial^2 u_m}{\partial t^2} \pm C\frac{\partial^2 u_m}{\partial x \partial t} - \frac{1}{2}C^2\frac{\partial^2 u_m}{\partial y^2} = 0, \tag{13}$$

$$\frac{\partial^2 v_m}{\partial t^2} \pm C\frac{\partial^2 v_m}{\partial y \partial t} - \frac{1}{2}C^2\frac{\partial^2 v_m}{\partial x^2} = 0, \tag{14}$$

where C is the constant phase speed of the waves leaving the domain.

The numerical scheme adopted in this work uses only two time levels hence time derivatives must not exceed the first order. To meet this requirement the above equations are split as

$$\frac{\partial u_m}{\partial t} \pm C\frac{\partial u_m}{\partial x} = R, \quad \frac{\partial R}{\partial t} - \frac{1}{2}C^2\frac{\partial^2 u_m}{\partial y^2} = 0, \tag{15}$$

$$\frac{\partial v_m}{\partial t} \pm C\frac{\partial v_m}{\partial y} = S, \quad \frac{\partial S}{\partial t} - \frac{1}{2}C^2\frac{\partial^2 v_m}{\partial x^2} = 0. \tag{16}$$

Unless some simplifications are introduced the transformation of Eqs. (15) and (16) to the curvilinear coordinates results in complicated expressions. Assuming an unvarying geometry for the physical domain in the vicinity of the outgoing boundary simplifies the process considerably by making the derivatives of the metrics zero. With the implementation of this plausible assumption and through appropriate combination of the equations the second-order radiation condition of Engquist and Majda [15] in curvilinear coordinates for the ξ- and η-directions becomes

$$\begin{aligned}
&(\xi_x\eta_y - \xi_y\eta_x)\frac{\partial U_m^*}{\partial \tau} + C\left[\left(\xi_x^2\eta_y - \xi_y^2\eta_x\right)\frac{\partial U_m^*}{\partial \xi} + \eta_x\eta_y(\xi_x - \xi_y)\frac{\partial U_m^*}{\partial \eta}\right] \\
&\quad - C\xi_x\xi_y\left[(\xi_x - \xi_y)\frac{\partial V_m^*}{\partial \xi} + (\eta_x - \eta_y)\frac{\partial V_m^*}{\partial \eta}\right] = \xi_x R + \xi_y S \\
&\frac{\partial R}{\partial \tau} - \frac{1}{2}C^2\left(\eta_y^3\frac{\partial^2 U_m^*}{\partial \eta^2} + 2\xi_y\eta_y^2\frac{\partial^2 U_m^*}{\partial \xi \partial \eta} + \xi_y^2\eta_y\frac{\partial^2 U_m^*}{\partial \xi^2}\right) \\
&\quad + \frac{1}{2}C^2\left(\xi_y\eta_y^2\frac{\partial^2 V_m^*}{\partial \eta^2} + 2\xi_y^2\eta_y\frac{\partial^2 V_m^*}{\partial \xi \partial \eta} + \xi_y^3\frac{\partial^2 V_m^*}{\partial \xi^2}\right) = 0,
\end{aligned} \tag{17}$$

$$\begin{aligned}
&(\xi_x\eta_y - \xi_y\eta_x)\frac{\partial V_m^*}{\partial \tau} + C\left[\left(\xi_x\eta_y^2 - \xi_y\eta_x^2\right)\frac{\partial V_m^*}{\partial \eta} - \xi_x\xi_y(\eta_x - \eta_y)\frac{\partial V_m^*}{\partial \xi}\right] \\
&\quad + C\eta_x\eta_y\left[(\eta_x - \eta_y)\frac{\partial U_m^*}{\partial \eta} + (\xi_x - \xi_y)\frac{\partial U_m^*}{\partial \xi}\right] = \eta_x R + \eta_y S \\
&\frac{\partial S}{\partial \tau} - \frac{1}{2}C^2\left(\xi_x^3\frac{\partial^2 V_m^*}{\partial \xi^2} + 2\xi_x^2\eta_x\frac{\partial^2 V_m^*}{\partial \xi \partial \eta} + \xi_x\eta_x^2\frac{\partial^2 V_m^*}{\partial \eta^2}\right) \\
&\quad + \frac{1}{2}C^2\left(\xi_x^2\eta_x\frac{\partial^2 U_m^*}{\partial \xi^2} + 2\xi_x\eta_x^2\frac{\partial^2 U_m^*}{\partial \xi \partial \eta} + \eta_x^3\frac{\partial^2 U_m^*}{\partial \eta^2}\right) = 0.
\end{aligned} \tag{18}$$

While Eqs. (17) and (18) provide definitely better absorption of directional waves, numerical experiments have revealed that their degenerate forms with $R = 0$ and $S = 0$ (Sommerfeld's equations) give almost identical results if the outgoing waves do not make acute angles with the boundary.

4. Numerical approach

Regardless of the shape of the physical domain, Eqs. (10)–(12) are solved in a perfectly rectangular computational domain using finite-difference approximations with unit grid sizes in both directions. If the physical domain is complicated the computational domain may be arranged as a combination of several rectangular domains (see for instance Bao et al. [10]). Several different approaches based on the staggered or non-staggered grids are available. After trying three different grid orientations (i.e., non-staggered grid, staggered Arakawa B-grid, and staggered Arakawa C-grid [17]) it has been decided that staggered Arakawa C-grid performed best for the equations used here. Fig. 2 shows the grid orientation for the variables.

Unlike Boussinesq models, which rely on higher derivative terms for better dispersion characteristics, the present wave model improves its dispersion by increasing the number of components ($n = 1, \ldots, N$) rather than increasing the order of derivatives of the dependent variables, hence contains at most second-order spatial derivatives. Therefore, the second-order accurate finite-difference approximations, widely used in many applications involving similar problems, are considered sufficient from the numerical point of view. Tests presented in the next section also support this choice. Accordingly, all the derivatives are second-order accurate and centered at the mid-time level $t + \Delta t/2$, t being the current time and Δt the time step. The main wave propagation direction is taken along the positive ξ-axis; therefore, ξ-momentum equation is solved first to obtain U_m^* for the new time level $t + \Delta t$, assuming the new time level values of ζ and V_m^* known. Then, η-momentum equation is solved for V_m^* using the new U_m^* values as computed from the previous step. The velocity computations require solutions of block tridiagonal matrix systems, which are accomplished very efficiently by the method first introduced by Keller [18] as a generalization of the Thomas algorithm. The surface displacement is obtained from a semi-explicit discretization (i.e. explicit in ζ, implicit in U_m^* and V_m^*) of the continuity equation, which is treated as explicit in the computations. Finally, the radiation condition is implemented through one-sided discretization of the spatial derivatives wherever needed; otherwise they are centered following the usual approach. Since all these computations involve certain approximations, an iterative procedure is needed. Through numerical experiments it has been

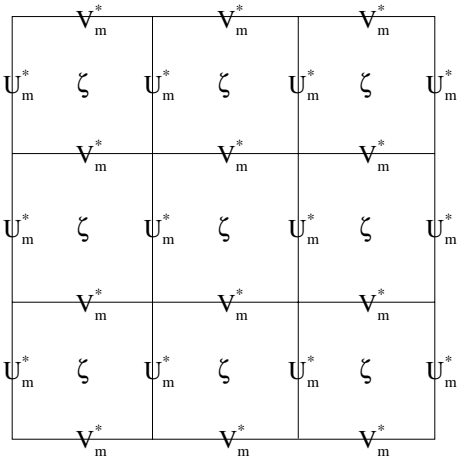

Fig. 2. Grid orientation for the variables ζ, U_m^*, and V_m^*.

ascertained that for all the cases considered in this work, a maximum of three iterations for linear computations and five iterations for nonlinear computations were sufficient to obtain reliable results. This was determined by continuously computing the difference between the iteratively computed values of the normalized surface displacement (normalized with respect to the incident wave amplitude) at every discreet point and requiring that the difference be less than 10^{-5}.

5. Test cases

For testing the reliability of the numerical scheme developed, two different simulations with known exact solutions are considered. The first case is the linear long wave propagation in a gradually converging and then diverging channel. The second case is the simulation of a linear random wave field in a circular channel.

5.1. Linear long waves in a channel of varying width

First, linear long wave propagation across a converging and then diverging channel is simulated and the variation of the wave amplitude along the channel length is compared with the theoretical formula of Green. The period of the incident wave is $T = 10$ s and the water depth is $h = 1$ m which result in a depth to wavelength ratio of approximately $h/L = 1/30$, indicating a long wave. The channel width at $x = 0$ is $b_0 = 20$ m, which reduces to half its value after a distance of five wavelengths and then widens to b_0 again after another five wavelengths, the channel width varying elliptically. For a gradually varying channel cross-section Green's formula (see Lamb [19], Section 185) predicts an amplitude variation according to

$$a(x) = a_0\sqrt{b_0/b(x)}, \tag{19}$$

where a_0 and b_0 are, respectively, the wave amplitude and the channel width at $x = 0$ while $a(x)$ and $b(x)$ are the corresponding values at an arbitrary location x along the channel. Simulations were performed for $N = 1$ component with $\omega_1 = 2\pi/T$. Time and space resolutions were $\Delta t = T/40$ s and $\Delta x = L/40$ m, $\Delta y = b(x)/40$ m, making the Courant number $Cr = C\Delta t/\Delta x$ exactly one. Eq. (17) with $R = 0$ and $S = 0$ was used as the radiation condition at $x = 10L$ m. The grids in the physical domain were not orthogonal since they were generated by simply making equal and straight divisions in the x-direction and then dividing the corresponding widths into equal lengths. Hence, the simulation also works as a check on the non-orthogonal terms. Fig. 3 shows a perspective view of the fully developed wave field and the comparison of the numerically computed wave form with Green's formula along the mid-section.

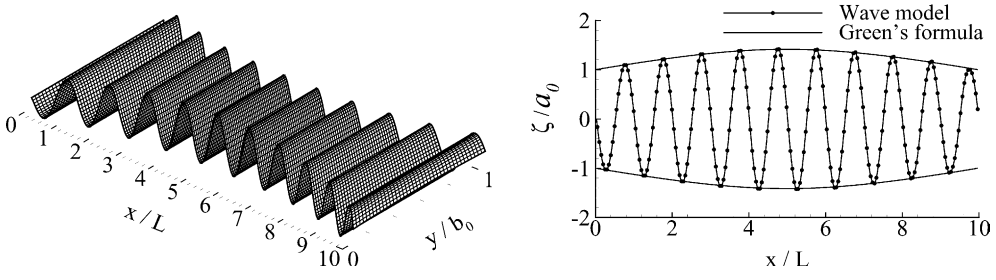

Fig. 3. Linear long wave propagation across an elliptically varying channel: perspective view (left) and variation of the simulated wave along the mid-section compared with the analytical formula (right). Surface displacement is normalized with respect to the incident wave amplitude.

5.2. Linear random waves in a circular channel

In the context of acoustics, Rostafinski [20] studied the sound propagation in a curved duct. The analytical solution, which may be readily adapted to the present problem, is as follows. Surface elevation in polar coordinates (r,θ) is expressed as a linear combination of different modes, which are given in terms of the Bessel functions of the first and second kind. The solution may be generalized to random waves by employing the principle of superposition so that the resultant surface elevation is expressed as

$$\zeta(r,\theta,t)=\sum_{p=1}^{P}\sum_{q=1}^{Q}\left[a_{pq}J_{\nu_{pq}}(k_p r)+b_{pq}Y_{\nu_{pq}}(k_p r)\right]\mathrm{e}^{\mathrm{i}\nu_{pq}\theta}\,\mathrm{e}^{\mathrm{i}(2\pi f_p t+\delta_p)}, \tag{20}$$

where i is the imaginary unit, f_p is the frequency of the pth component of the random wave field composed of P components, k_p and δ_p are the corresponding wavenumber and the random phase angle, respectively. a_{pq} and b_{pq} are the amplitudes which depend on both the solution mode and the imposed spectral shape, and finally ν_{pq} is the order of the Bessel functions which is to be computed from Eq. (23), whose number of roots determines the total number of modes Q for each wave component p.

The boundary conditions on the inner wall $\partial\zeta/\partial r|_{r=r_i}=0$ and outer wall $\partial\zeta/\partial r|_{r=r_o}=0$ give, respectively,

$$a_{pq}J'_{\nu_{pq}}(k_p r_i)+b_{pq}Y'_{\nu_{pq}}(k_p r_i)=0, \tag{21}$$

$$a_{pq}J'_{\nu_{pq}}(k_p r_o)+b_{pq}Y'_{\nu_{pl}}(k_p r_o)=0, \tag{22}$$

in which the primes denote differentiation with respect to r while r_i and r_o denote the inner and outer radii of the circular channel. From Eqs. (21) and (22) the following condition is obtained for determining ν_{pq}:

$$J'_{\nu_{pq}}(k_p r_i)Y'_{\nu_{pq}}(k_p r_o)-J'_{\nu_{pq}}(k_p r_o)Y'_{\nu_{pq}}(k_p r_i)=0. \tag{23}$$

The incident wave amplitudes for each pth wave component are determined according to the specified spectral shape. Imposing the incident wave amplitude as $\zeta(r,0,t)=\sum_{p=1}^{P}c_p\exp[\mathrm{i}(2\pi f_p t+\delta_p)]$ at the channel entrance $\theta=0$, noting that each component function is orthogonal with weight $1/r$, the coefficients a_{pq} and b_{pq} are computed as

$$a_{pq}=c_p Y'_{\nu_{pq}}(k_p r_i)\frac{\int_{r_i}^{r_o}\frac{F_{pq}(r)}{r}\,\mathrm{d}r}{\int_{r_i}^{r_o}\frac{F_{pq}^2(r)}{r}\,\mathrm{d}r},\quad b_{pq}=-a_{pq}\frac{J'_{\nu_{pq}}(k_p r_i)}{Y'_{\nu_{pq}}(k_p r_i)}, \tag{24}$$

where $F_{pq}(r)=J_{\nu_{pq}}(k_p r)Y'_{\nu_{pq}}(k_p r_i)-Y_{\nu_{pq}}(k_p r)J'_{\nu_{pq}}(k_p r_i)$ is obtained by solving (21) for b_{pq} and then substituting it into (20). Note that b_{pq} could be obtained from Eq. (22) as well.

For the test case considered here the inner radius of the channel is taken as $r_i=50$ m and the outer radius as $r_o=100$ m; the channel covers an arc of 180°. The water depth and the incident mean wave period are selected as $h=5$ m and $T_m=5$ s, respectively. Component wave amplitudes c_p of the incident waves are specified according to the shape of a Bretshneider spectrum. Random phases are generated in the range of $0-2\pi$ using a random number generator subroutine. $P=50$ sinusoidal waves with amplitudes c_p and frequencies $f_p=pf_c/P$, $f_c=1.5/T_m$ being the cutoff frequency, are imposed across the channel at the entrance while Eq. (17) is used as the radiation condition at the end of the computational domain. To avoid numerical problems associated with the Bessel functions for high wavenumbers and high orders in Eq. (23) the cutoff frequency is necessarily limited.

Since the incident waves are random, wave model in curvilinear coordinates was run for two wave components $N=2$ with circular frequencies $\omega_1=2\pi/T_m$ and $\omega_2=2\omega_1$. In the physical domain, a constant angular grid spacing of $\Delta\theta=\pi/400$ rad was used along the channel while the grid spacing in the radial

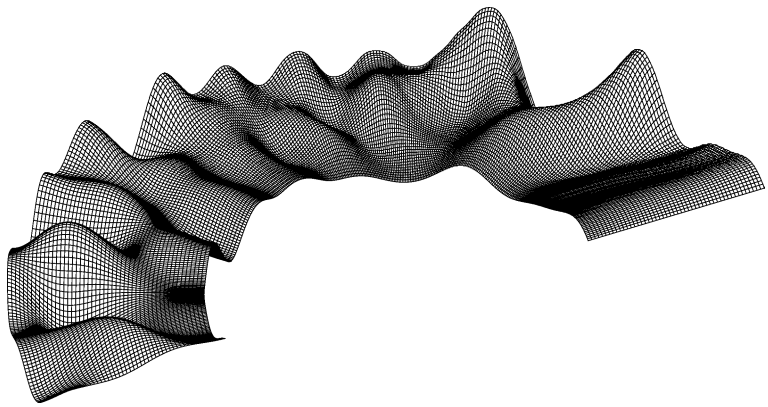

Fig. 4. Perspective view of random wave propagation in a circular channel at $t = 18T_m$ s as obtained from the numerical solution of the present model.

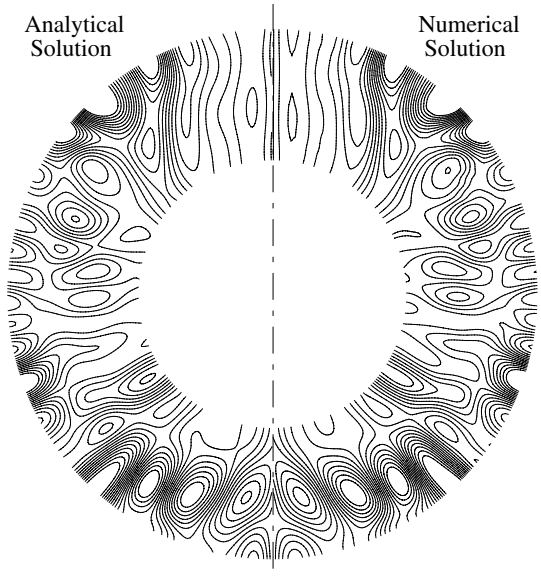

Fig. 5. Contour lines of the fully developed random wave field in a circular channel: analytical solution (left) and numerical solution at $t = 18T_m$ s (right).

direction was $\Delta r = 1$ m. Time resolution was taken as $\Delta t = T_m/50$ s so that the average Courant number (computed by averaging the arc lengths corresponding to the inner and outer radii) in the wave propagation direction was approximately unity.

As the waves propagate in the circular channel, they reflect from the outer wall and diffract in the vicinity of the inner wall thus creating quite complicated patterns as shown in the perspective view at $t = 18T_m$ s in Fig. 4. In order to make comparisons with the theory presented above, the contours of the analytical solution and the fully developed wave field as obtained from the numerical solution after 18 wave periods elapsed are depicted together in Fig. 5. Finally, comparisons of the surface displacement between the analytical and numerical solution along the inner wall and the outer wall are presented in Figs. 6(a) and (b).

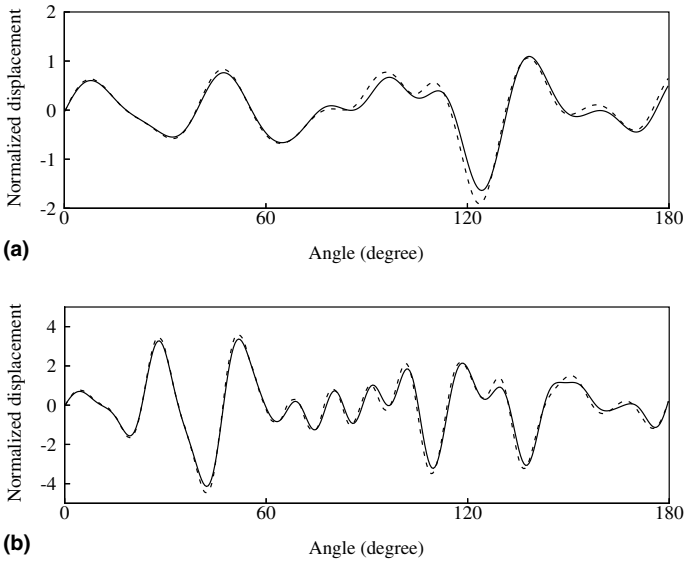

Fig. 6. Comparison of the analytical solution (solid line) with the numerical solution at $t = 18T_m$ s (dashed line) for the normalized surface displacement along the inner wall (a) and outer wall (b) of the circular channel.

Except for minor differences the two solutions remarkably agree with each other and establish confidence in the model equations and the numerical code.

6. Nonlinear wave simulations

The wave model used in this work is capable of reproducing the well-known periodic small-amplitude waves both in shallow water and in deep water equally well. Simulations of cnoidal and Stokes waves in a circular channel are presented now as examples to nonlinear wave transformations within curved boundaries.

6.1. Cnoidal waves in a circular channel

Cnoidal waves are nonlinear periodic shallow water waves formulated first by Korteweg and DeVries [21] in connection with the wave equation they derived. According to the cnoidal wave theory only two dimensionless parameters may be selected freely; the rest of the physical quantities, such as wave period, wavelength, and celerity are fixed according to these two parameters and the complete elliptic integrals of $E(m)$ and $K(m)$ which depend on m. In principle it is possible to select a definite period and wavelength, and then determine the corresponding wave steepness and modulus, but this approach is quite tedious due to the dependency of $E(m)$ and $K(m)$ on m (see [22, p. 547]). Therefore, in the simulations presented here, two different wave steepness H/h (H wave height) values and modulus m are selected first, and then, taking the water depth $h = 3$ m, the remaining physical quantities T, L, C and the surface displacement ζ are computed according to the original cnoidal theory [21]. Due to the reduced water depth, the depth to the wavelength ratio now confirms the necessary long wave condition. Because of the reflections from the outer wall, waves become quite steep (as much as four times the incident amplitude) therefore moderate wave steepness values $H/h = 0.1$ and $H/h = 0.3$ are used for the incoming waves. The modulus m for each wave steepness H/h is

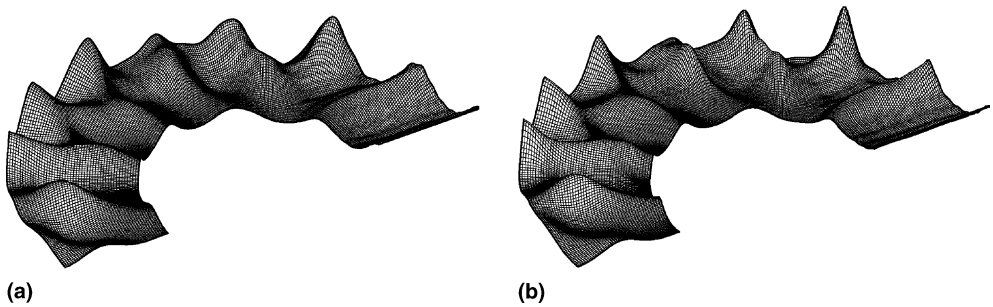

Fig. 7. Perspective views of the fully developed cnoidal wave fields at $t = 18T$ s in a circular channel for $H/h = 0.1$ (a) and $H/h = 0.3$ (b). Surface displacement is normalized with respect to half the incident wave height.

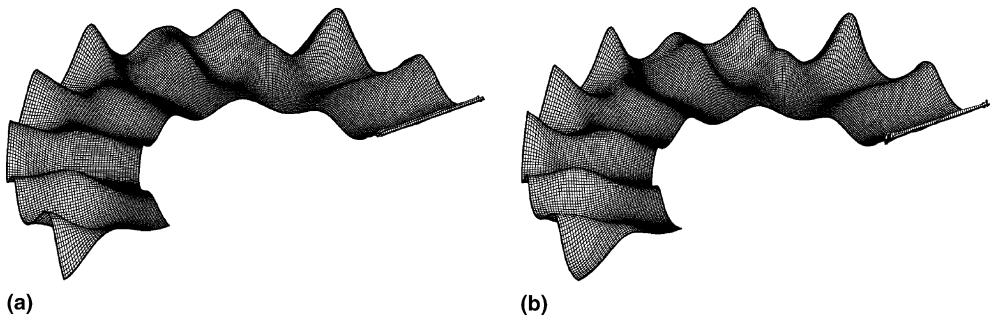

Fig. 8. Perspective views of the fully developed Stokes wave fields at $t = 18T$ s in a circular channel for $kH = 0.1$ (a) and $kH = 0.3$ (b). Surface displacement is normalized with respect to half the incident wave height.

determined by trial and error in such a way as to make the wavelength the same for both cases, which in turn is the same as the mean wavelength of the linear test case given in Section 6.1. Accordingly, $m = 0.54$ for $H/h = 0.1$ and $m = 0.89$ for $H/h = 0.3$ are used. Numerical conditions (time and space resolutions, etc.) are identical to those used in the linear simulations.

Since the dimensions of the circular channel is kept the same for all (linear and nonlinear) simulations it is aimed to maintain a geometric similarity by keeping the wavelength the same as well, for all the cases. In this way it is possible to observe the prominent features and effects of nonlinearity which arise principally from the high wave steepness. Figs. 7(a) and (b) show the fully developed wave fields for two different wave steepness values. As expected, $H/h = 0.1$ case, being rather weak in nonlinearity, resembles the linear case; however, as the wave steepness becomes higher $H/h = 0.3$, due to the asymmetric form of the waves, reflections from the outer wall increase considerably and the patterns become sharper.

6.2. Stokes waves in a circular channel

Since Stokes waves are essentially deep water waves, the wave steepness is measured by kH. Similar to the cnoidal wave simulations, two different steepness values $kH = 0.1$ and $kH = 0.3$ are selected for simulations. The circular channel dimensions and the water depth are kept the same as the linear test case, the wave periods for each steepness values are adjusted so that the wavelengths for both cases would be the same as the other simulations. The incident wave form is specified according to the second-order Stokes theory. Because the Stokes waves are asymmetric compared to the linear waves but not as asymmetric as the cnoidal waves, the resulting wave patterns are expectedly between those of the linear and of the cnoidal

waves. Figs. 8(a) and (b) show the fully developed wave fields for the wave steepness values $kH = 0.1$ and $kH = 0.3$, respectively. Obviously, the case of $kH = 0.3$ has sharper features but the contrasts between the two figures are not as prominent as those of the cnoidal waves.

7. Concluding remarks

Fully dispersive nonlinear wave equations in curvilinear coordinates with non-orthogonal grids have been developed based on the wave model of Nadaoka et al. [16], which is valid for broad-banded nonlinear waves in arbitrary relative depths. Finite-difference approximations with a staggered grid system (Arakawa C-grid) is adopted for the numerical solution of the resulting boundary-fitted wave equations. Comparisons for the test cases of a gradually varying channel and a circular channels provide convincing evidence regarding the reliability and accuracy of the model equations and the numerical approach. The cnoidal and Stokes waves in a circular channel are also simulated for two different wave steepness values to demonstrate the model's capability of simulating nonlinear waves as well as revealing the prominent features of nonlinear wave patterns. Treatment of more complicated regions is also possible by an appropriate generation of grids that results in not a single rectangular computational domain but a combination of rectangular domains. The future work aims at concentrating on the applications of the present equations to practical case studies of natural or man-made areas.

Acknowledgements

The first author gratefully acknowledges the financial support provided by the Kajima Foundation of Japan which made this work possible.

References

[1] J.F. Thompson, Z.U.A. Warsi, C.W. Mastin, Numerical Grid Generation – Foundations and Applications, North-Holland, Amsterdam, 1985.
[2] K.A. Hoffmann, S.T. Chiang, Computational Fluid Dynamics for Engineers (third print), vols. 1 and 2, Engineering Education System, Wichita, KS, 1995.
[3] B.H. Johnson, VAHM-A vertically averaged hydrodynamic model using boundary-fitted coordinates. MP HL-80-3 US Army Engrs. Wtrwy. Experiment St., Vicksburg, Miss. 1980.
[4] M.L. Spaulding, A vertically averaged circulation model using boundary-fitted coordinates, J. Phys. Oceanogr. 14 (1984) 973–982.
[5] J.B.T.M. Willemse, G.S. Stelling, G.K. Verbroom, Solving the shallow water equations with an orthogonal coordinate transformation. Delft Hydr. Communication No. 356. Delft Hydraulics Laboratory, Delft, The Netherlands, 1985.
[6] M. Muin, M. Spaulding, Two-dimensional boundary-fitted circulation model in spherical coordinates, J. Hydr. Eng. (September) (1996) 512–521.
[7] Y.P. Sheng, Numerical modeling of coastal and estuarine processes using boundary-fitted grids, 3rd Int. Symp. River Sedimentation (1986) 1426–1442.
[8] A.A. Androsov, K.A. Klevanny, E.S. Salusti, N.E. Voltzinger, Open boundary conditions for horizontal 2-D curvilinear-grid long-wave dynamics of a strait, Adv. Water Resour. 18 (1995) 267–276.
[9] F. Shi, W. Sun, G. Wei, A WDM method on a generalized curvilinear grid for calculation of storm surge flooding, Appl. Ocean Res. 19 (1997) 275–282.
[10] X.W. Bao, J. Yan, W.X. Sun, A three-dimensional tidal wave model in boundary-fitted curvilinear grids, Estuar., Coast. Shelf Sci. 50 (2000) 775–788.
[11] Y.S. Li, J.M. Zhan, Boussinesq-type model with boundary-fitted coordinate system, J. Wtrwy. Port Coastal Ocean Eng. 127 (3) (2001) 152–160.
[12] F. Shi, R.A. Dalrymple, J.T. Kirby, Q. Chen, A. Kennedy, A fully-nonlinear Boussinesq model in generalized curvilinear coordinates, Coast. Eng. 42 (2001) 337–358.

[13] D.A. Romanenkov, A.A. Androsov, N.E. Voltzinger, Comparison of forms of the viscous shallow-water equations in the boundary-fitted coordinates, Ocean Model. 3 (2001) 193–216.
[14] S. Sankaranarayanan, M.L. Spaulding, A study of the effects of grid non-orthogonality on the solution of shallow water equations in boundary-fitted coordinate sytems, J. Comput. Phys. 184 (2003) 299–320.
[15] B. Engquist, A. Majda, Absorbing boundary conditions for the numerical simulation of waves, Math. Comp. 31 (1977) 629–651.
[16] K. Nadaoka, S. Beji, Y. Nakagawa, A fully dispersive weakly nonlinear model for water waves, Proc. R. Soc. Lond. A 453 (1997) 303–318.
[17] A. Arakawa, V.R. Lamb, Computational design of the basic dynamical processes of the UCLA general circulation model, Meth. Comput. Phys. 17 (1977) 174–265.
[18] H.B. Keller, Accurate difference methods for nonlinear two-point boundary value problems, SIAM J. Num. Anal. 11 (1974) 305–320.
[19] H. Lamb, Hydrodynamics, Dover, New York, 1932, p. 738.
[20] W. Rostafinski, Acoustic systems containing curved duct sections, J. Acoust. Soc. Am. 60 (1976) 23–28.
[21] D.J. Korteweg, G. De Vries, On the change of form of long waves advancing in a rectangular canal, and on a new type of long stationary waves, Philos. Mag. 39 (1895) 422–443.
[22] C.C. Mei, The Applied Dynamics of Ocean Surface Waves, World Scientific, Singapore, 1989.